



## Synthesis of microsphere silicon carbide/nanoneedle manganese oxide composites and their electrochemical properties as supercapacitors



Myeongjin Kim <sup>a</sup>, Youngjae Yoo <sup>b,\*,\*\*</sup>, Jooheon Kim <sup>a,\*</sup>

<sup>a</sup> School of Chemical Engineering & Materials Science, Chung-Ang University, Seoul 156-756, South Korea

<sup>b</sup> Division of Advanced Materials, Korea Research Institute of Chemical Technology, Daejeon 305-600, South Korea

### HIGHLIGHTS

- Oxygen-containing functional groups are introduced on the SiC surface.
- Nanoneedle MnO<sub>2</sub> is formed on the SiC surface using functional groups.
- SiC/nanoneedle MnO<sub>2</sub> composites are studied as cathode for capacitor in 1 M Na<sub>2</sub>SO<sub>4</sub>.
- The material has specific capacitance of 273.2 F g<sup>-1</sup> with a scan rate of 10 mV s<sup>-1</sup>.

### ARTICLE INFO

#### Article history:

Received 25 February 2014

Received in revised form

23 April 2014

Accepted 25 April 2014

Available online 6 May 2014

#### Keywords:

Supercapacitors

Silicon carbide

Nanoneedle manganese oxide

Pseudocapacitance

Hybrid electrode materials

Oxygen functional groups

### ABSTRACT

Synthesis of microsphere silicon carbide/nanoneedle MnO<sub>2</sub> (SiC/N–MnO<sub>2</sub>) composites for use as high-performance materials in supercapacitors is reported herein. The synthesis procedure involves the initial treatment of silicon carbide (SiC) with hydrogen peroxide to obtain oxygen-containing functional groups to provide anchoring sites for connection of SiC and the MnO<sub>2</sub> nanoneedles (N–MnO<sub>2</sub>). MnO<sub>2</sub> nanoneedles are subsequently formed on the SiC surface. The morphology and microstructure of the as-prepared composites are characterized via X-ray diffractometry, field-emission scanning electron microscopy, thermogravimetric analysis, and X-ray photoelectron spectroscopy. The characterizations indicate that MnO<sub>2</sub> nanoneedles are homogeneously formed on the SiC surface in the composite. The capacitive properties of the as-prepared SiC/N–MnO<sub>2</sub> electrodes are evaluated using cyclic voltammetry, galvanostatic charge/discharge testing, and electrochemical impedance spectroscopy in a three-electrode experimental setup using a 1-M Na<sub>2</sub>SO<sub>4</sub> aqueous solution as the electrolyte. The SiC/N–MnO<sub>2</sub>(5) electrode, for which the MnO<sub>2</sub>/SiC feed ratio is 5:1, displays a specific capacitance as high as 273.2 F g<sup>-1</sup> at 10 mV s<sup>-1</sup>.

© 2014 Elsevier B.V. All rights reserved.

## 1. Introduction

Over the past few years, rapid development of methods for harnessing renewable energy (e.g., solar and wind energy) has increased the need for sustainable energy storage technologies to address the challenges of increasing energy demand and the cyclic nature of renewable energy sources [1–4]. The high power density, moderate energy density, good operational safety, and long cycling life of electrochemical double layer capacitors or supercapacitors have fueled extensive exploration of these promising technologies

for various emerging energy applications such as in high-power electronic devices, electric vehicles, and hybrid electric vehicles [5–7].

Generally, supercapacitors can be classified into one of the two categories based on their energy storage mechanism: electric double layer capacitors (EDLCs) and pseudocapacitors [8,9]. High surface area carbon has typically been used as an electrode material for EDLC given that it is convenient for storing energy in a double layer formed on the electrode surface. Conversely, most of the electrode materials used in pseudocapacitors consist of conductive polymers and metal oxides, which transfer faradic charges between an electrolyte and electrode. Therefore, to enhance the energy density of supercapacitors, many researchers have utilized hybrid materials in which the electrode materials for EDLCs are combined with other redox

\* Corresponding author. Tel.: +82 2 820 5763; fax: +82 2 812 3495.

\*\* Corresponding author. Tel.: +82 42 860 7216; fax: +82 42 861 4151.

E-mail addresses: [yjyoo@kRICT.re.kr](mailto:yjyoo@kRICT.re.kr) (Y. Yoo), [jooheonkim@cau.ac.kr](mailto:jooheonkim@cau.ac.kr) (J. Kim).

pseudo-capacitive materials [10,11]; however, most of the research has focused on the application of the combination of graphene with metal oxides or a conductive polymer [12–15].

Recently, novel approaches have been proposed for application of semiconductor or cermet nanowires as EDLC electrode materials instead of traditional carbon materials such as activated carbons, aerogels, carbon nanotubes, and graphene. The application of silicon nanowires, silicon carbide nanowires, titanium nitride nanowires, and titanium dioxide nanotubes and nanowires as EDLC electrode materials has attracted much attention because these materials offer the merits of high specific surface area and electrical conductivity [16–21]. However, these materials are suitable for micro-supercapacitor electrodes because the working materials are grown directly on the current collector. In this regard, there is no literature on the application of semiconductor or cermet nanowires for use in macroscale supercapacitors as EDLC electrode materials. Furthermore, hybrid composites that combine semiconductor and redox pseudocapacitive materials have not been reported.

Metal oxide electrode materials are particularly attractive for redox pseudo-capacitive materials due to their high capacitance and fast redox kinetics. Manganese oxide ( $MnO_2$ ) has been distinguished as the most promising transition metal oxide for next generation supercapacitors due to its high energy density, low cost, environmental friendliness, and natural abundance [22,23]. Some studies have attempted to achieve enhanced specific capacitance by preparation of  $MnO_2$  with different morphologies in order to increase the specific area of  $MnO_2$ . Based on synthesis of  $MnO_2$  with different crystallographic forms ( $\alpha$ ,  $\gamma$ ) and morphologies (needles, rods, and spindles) and evaluation of their electrochemical performance, Chen et al. reported that needle-like  $MnO_2$  samples exhibited greater specific capacitance than the other forms [24]. Similarly, Devaraj and Munchandraiah investigated the effect of the crystallographic structure of  $MnO_2$  on its electrochemical capacitance properties and found that  $MnO_2$  with  $\alpha$ - and  $\delta$ -crystallographic structures exhibited greater specific capacitance [25].

Chen et al. successfully created electrode materials by combining graphene oxide (GO) with nanoneedle  $MnO_2$  for application of nanoneedle  $MnO_2$  and electrode combination materials to EDLCs, and demonstrated that nanoneedle  $MnO_2$  can be homogeneously dispersed on GO sheets using various functional groups [26]. Kim et al. suggested the use of activated carbon/nanoneedle  $MnO_2$  composites obtained using oxygen-containing functional groups that were introduced by thermal treatment of activated carbon [27]. On the basis of their research, oxygen-containing functional groups appear to be essential for fabricating carbon-based EDLC materials/nanoneedle  $MnO_2$  composites because the functional groups act as anchor sites enabling the homogeneous attachment of nanoneedle  $MnO_2$  to the surface of the EDLC materials.

We report herein, the synthesis of microsphere silicon carbide and nanoneedle  $MnO_2$  composites based on the anticipation that the nanoneedle  $MnO_2$  should promote reversible pseudocapacitance of electrodes constructed from the composite, whereas silicon carbide should act as the support for the formation of  $MnO_2$  nanoneedles and the electronic conductive channels, thereby impacting the electrical double layer properties. The strategy involves creating oxygen-containing functional groups as anchorage sites for connecting the silicon carbide and  $MnO_2$  nanoneedles to obtain a homogeneous dispersion of  $MnO_2$  by treating silicon carbide with hydrogen peroxide. The morphology and microstructural characteristics of the silicon carbide/ $MnO_2$  nanoneedle composites are investigated in detail, and the electrochemical performance of each composite is also investigated on the basis of cyclic voltammetry (CV), galvanostatic charge/discharge experiments, and electrochemical impedance spectroscopy (EIS). The specific capacitance and capacitance retention are also analyzed.

## 2. Experimental

### 2.1. Raw materials

The microsphere silicon carbide (the average particle diameter, 30  $\mu\text{m}$ ; >99% purity) used in this study were supplied by LG Innotek (Ansan, Korea). Hydrofluoric acid (HF, HPLC grade, Samchun Chemical, Pyungteak, Korea), Hydrogen peroxide ( $H_2O_2$ , HPLC grade, Samchun Chemical, Pyungteak, Korea), Isopropyl alcohol (IPA, HPLC grade, Samchun Chemical, Pyungteak, Korea) and *N*-methylpyrrolidone (NMP, HPLC grade, Samchun Chemical, Pyungteak, Korea) were used as received. Manganese(II) chloride tetrahydrate ( $MnCl_2 \cdot 4H_2O$ , Aldrich, Seoul), Potassium permanganate ( $KMnO_4$ , Aldrich, Seoul), Poly(vinylidenefluoride) (PVDF, Aldrich, Seoul) and deionized water (DI water, HPLC grade, Aldrich, Seoul) were purchased from Sigma Chemical. All of the chemicals were used without further purification.

### 2.2. Synthesis of silicon carbide/ $MnO_2$ composites

The residual  $SiO_2$  layer adsorbed on the surface of the microsphere SiC particles was removed by treatment with hydrofluoric acid (HF). In a typical synthesis, 120 g of SiC powder (hereafter, Raw SiC) was placed in 300 mL of 10% HF solution and stirred for 24 h. Subsequently, the sample was leached with distilled water until the pH of the leaching water reached 7–8. These samples were denoted as HF–SiC. In order to introduce the oxygen-containing functional groups on the SiC surface, HF-treated SiC powder was dispersed in a 34% hydrogen peroxide ( $H_2O_2$ ) solution and heated to 85 °C for 24 h with vigorous stirring. The resulting mixture was filtered, washed several times, and dried in a vacuum oven at 60 °C for 24 h. The resulting products were denoted as  $H_2O_2$ –SiC. The  $H_2O_2$ -treated microsphere silicon carbide/nanoneedle  $MnO_2$  (SiC/N– $MnO_2$ ) composite produced using a  $MnO_2$ /SiC feed ratio of 1:1 (SiC/N– $MnO_2$ (1)) was synthesized as follows: SiC (0.05 g) and  $MnCl_2 \cdot 4H_2O$  (0.068 g) were dispersed in isopropyl alcohol (50 mL) with ultrasonication for 0.5 h. Subsequently, the mixture was heated to approximately 85 °C in a water-cooled condenser with vigorous stirring;  $KMnO_4$  (0.036 g) dissolved in 5 mL of DI water was then added to the boiling solution. The resulting mixture was filtered, washed several times, and dried in a vacuum oven at 60 °C for 24 h. The products were denoted as SiC/N– $MnO_2$ (1) and SiC/N– $MnO_2$ (5) corresponding to  $MnO_2$ /SiC feed ratios of 1:1 and 5:1, respectively.

### 2.3. Characterization methods

X-ray diffraction (XRD) patterns were collected (New D8-Advance/Bruker-AXS) at a scan rate of 1°  $\text{s}^{-1}$  within the 2 $\theta$  range 10°–80° using  $CuK_{\alpha 1}$  radiation (0.154056 nm). Field-emission scanning electron microscopy (FE-SEM, SIGMA, Carl Zeiss) was used to examine the morphology of the prepared samples. X-ray photoelectron spectroscopy (XPS) analysis was performed on a VGMicrotech ESCA2000 system using a spectrometer with a  $Mg K\alpha$  X-ray source (1253.6 eV) and a hemispherical analyzer. During the curve fitting, the Gaussian peak widths were constant in each spectrum. Thermogravimetric analysis (TGA) was performed on a TA Instruments TGA-2050 apparatus at a heating rate of 10 °C  $\text{min}^{-1}$  in air.

### 2.4. Preparation and characterization of supercapacitors

Working electrodes were fabricated as follows. First, the as-prepared materials and poly(vinylidenefluoride) (PVDF) were mixed in a mass ratio of 95:5 and dispersed in *N*-methylpyrrolidone (NMP). The resulting mixture was then coated onto a nickel foam

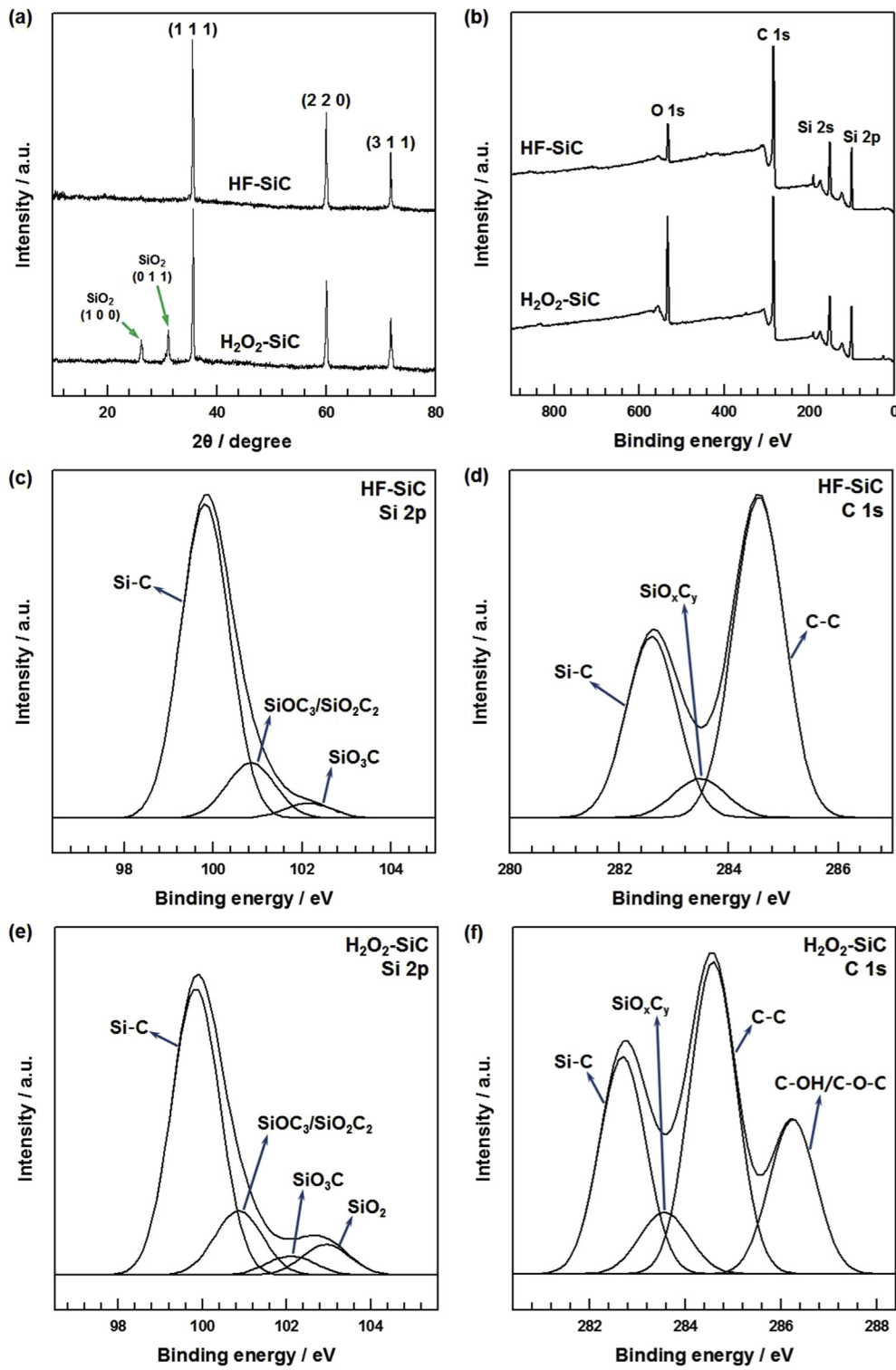


**Fig. 1.** (a) XRD patterns of HF–SiC and H<sub>2</sub>O<sub>2</sub>–SiC. (b) XPS wide scan survey spectra of HF–SiC and H<sub>2</sub>O<sub>2</sub>–SiC. (c) XPS deconvoluted Si 2p spectrum of HF–SiC. (d) XPS deconvoluted C 1s spectrum of HF–SiC. (e) XPS deconvoluted Si 2p spectrum of H<sub>2</sub>O<sub>2</sub>–SiC. (f) XPS deconvoluted C 1s spectrum of H<sub>2</sub>O<sub>2</sub>–SiC.

substrate (1 cm × 1 cm) and dried in a vacuum oven at 60 °C for 6 h. The loading mass of each electrode was approximately 2.7–3.2 mg. Cyclic voltammetry (CV), galvanostatic charge/discharge experiments, and electrochemical impedance spectroscopy (EIS) were performed in three-electrode mode using the as-prepared samples, platinum foil (1 cm × 1 cm), a Ag/AgCl (KCl-saturated) electrode as

the working electrode, a counter electrode, and a reference electrode in order to investigate the electrochemical behavior of the as-prepared samples. All measurements were performed in an aqueous electrolyte solution of 1 M Na<sub>2</sub>SO<sub>4</sub> at room temperature. Cyclic voltammetry (CV), galvanostatic charge/discharge, and electrochemical impedance spectroscopy (EIS) assays were

**Table 1**

The Si 2p peak position and the relative atomic percentages of various functional groups in HF–SiC and H<sub>2</sub>O<sub>2</sub>–SiC.

| Fitting of the Si 2p peak binding energy [eV]<br>(Relative atomic percentage [%]) |  |                    |                  |              |
|---|--|--------------------|------------------|--------------|
| Si–C  | SiOC <sub>3</sub> /SiO <sub>2</sub> C <sub>2</sub> | SiO <sub>3</sub> C | SiO <sub>2</sub> |              |
| HF–SiC  | 99.82 (81.6)                                       | 100.85 (14.5)      | 102.13 (3.9)     | –            |
| H <sub>2</sub> O <sub>2</sub> –SiC  | 99.84 (71.4)                                       | 100.86 (16.2)      | 102.11 (4.8)     | 102.92 (7.6) |

performed with a CHI 660C electrochemical workstation. EIS measurements were recorded under the following conditions: AC voltage amplitude: 5 mV, frequency range: 0.1–10<sup>5</sup> Hz, and open circuit potential.

### 3. Results and discussion

The protocol for synthesis of the SiC/N–MnO<sub>2</sub> composites involves three main steps: (i) removal of the residual SiO<sub>2</sub> layer adsorbed on the surface of the microsphere SiC particles by hydrofluoric acid leaching; (ii) hydrogen peroxide treatment of the HF-treated silicon carbide to create the oxygen-containing functional groups to provide sites for anchoring the MnO<sub>2</sub> nanoneedles to the silicon carbide; and (iii) formation of MnO<sub>2</sub> nanoneedles using various functional groups that were formed by the hydrogen peroxide treatment in an isopropyl alcohol–water solution. The proposed mechanism for the formation of nanoneedle MnO<sub>2</sub> on SiC can be illustrated by the following reaction: 2KMnO<sub>4</sub> + 3MnCl<sub>2</sub> + 2H<sub>2</sub>O → 5MnO<sub>2</sub> + 2KCl + 4HCl [26].

It is essential to confirm the successful introduction of oxygen-containing functional groups onto the SiC surface prior to the formation of MnO<sub>2</sub> nanoneedles. Fig. 1(a) shows the XRD patterns of hydrofluoric acid-treated SiC (HF–SiC) and hydrogen peroxide-treated SiC (H<sub>2</sub>O<sub>2</sub>–SiC). The XRD pattern of HF–SiC is consistent with the  $\beta$ -SiC phase (JCPDS 29–1129,  $a = 4.3589$  Å), indicated by diffraction peaks at  $2\theta = 35.6^\circ, 60^\circ$ , and  $71.7^\circ$ , assigned to the (1 1 1), (2 2 0), and (3 1 1) reflections, respectively [28,29]. However, after hydrogen peroxide treatment, several SiO<sub>2</sub> peaks are apparent for the microsphere SiC particle surface, as further confirmed by XPS analysis. Fig. 1(b) shows the XPS survey spectra of HF–SiC and H<sub>2</sub>O<sub>2</sub>–SiC. The survey spectrum of HF–SiC consists of only three elements, primarily C, O, and Si. However, the intensity of the O 1s signal increases dramatically in the spectrum of H<sub>2</sub>O<sub>2</sub>–SiC, indicating that oxygen-related functional groups are formed on the SiC surface. In order to obtain detailed information regarding the surfaces of HF–SiC and H<sub>2</sub>O<sub>2</sub>–SiC, the Si 2p and C 1s core level spectra of each sample are deconvoluted, and the results are shown in Fig. 1(c), (d), (e), and (f) and summarized in Tables 1 and 2. The Si 2p core level spectrum of HF–SiC (Fig. 1(c)) shows a strong Si–C peak at the binding energy of 99.8 eV and also indicates very low concentrations of some intermediate oxidation products such as SiOC<sub>3</sub> + SiO<sub>2</sub>C<sub>2</sub> at 100.8 eV and SiO<sub>3</sub>C at 102.1 eV. The C 1s core level spectrum (Fig. 1(d)) shows strong binding energy peaks of C–C bonds at 284.5 eV, with Si–C bonds at 282.6 eV and very low

intensity binding energy peaks of SiO<sub>x</sub>C<sub>y</sub> at 283.7 eV [30]. However, following hydrogen peroxide treatment, the areas of both the SiOC<sub>3</sub> + SiO<sub>2</sub>C<sub>2</sub> and SiO<sub>3</sub>C peaks increase slightly, and a SiO<sub>2</sub> peak is observed at a binding energy of 102.9 eV in the Si 2p spectrum (Fig. 1(e)). Moreover, a new peak corresponding to the C–OH/C–O–C groups emerges at 286.2 eV and the area of the SiO<sub>x</sub>C<sub>y</sub> peak also increases slightly in the C 1s spectrum (Fig. 1(f)), results that are in accordance with the behavior of the SiOC<sub>3</sub> + SiO<sub>2</sub>C<sub>2</sub> and SiO<sub>3</sub>C peaks in the Si 2p spectra (Fig. 1(e)). It can thus be concluded that oxygen-containing functional groups such as C–OH and C–O–C groups have been effectively introduced onto the SiC surface, resulting in anchorage sites for connection of the silicon carbide and the MnO<sub>2</sub> nanoneedles.

XRD analysis (Fig. 2) confirms the formation of the nanoneedle structure of  $\alpha$ -type MnO<sub>2</sub> on the SiC surface. The diffraction peaks of as-synthesized SiC/N–MnO<sub>2</sub>(5) are similar to those of the nanotetragonal phase of  $\alpha$ -MnO<sub>2</sub> (JCPDS 44–0141,  $a = 9.7845$ ,  $c = 2.8630$  Å), whereas diffraction peaks are nearly nonexistent in the XRD pattern of H<sub>2</sub>O<sub>2</sub>–SiC [31]. These observations indicate the formation of homogeneous composites in which the SiC surface is covered with needle-like nanoscale MnO<sub>2</sub>, a result that correlates well with previous studies in which the diffraction peaks of H<sub>2</sub>O<sub>2</sub>–SiC weaken or are absent [32].

Details of the surface morphology of H<sub>2</sub>O<sub>2</sub>–SiC and SiC/N–MnO<sub>2</sub>(5) are garnered from X-ray photoelectron spectroscopy (XPS), and the corresponding results are presented in Fig. 3. As shown in Fig. 3(a), the XPS survey spectrum of H<sub>2</sub>O<sub>2</sub>–SiC comprises only three elements: C, Si, and O. However, a signal corresponding to Mn (2p<sub>3/2</sub>, 2p<sub>1/2</sub>) emerges in the spectrum of SiC/N–MnO<sub>2</sub>(5), indicating that MnO<sub>2</sub> nanoneedles are successfully formed on the SiC surface. Moreover, the intensity of the C and Si peaks decreases dramatically because the MnO<sub>2</sub> nanoneedles fully cover the SiC surface, which is in accordance with the XRD analysis. Fig. 3(b) shows the Mn 2p core-level spectra of SiC/N–MnO<sub>2</sub>(5), where the Mn 2p<sub>3/2</sub> and Mn 2p<sub>1/2</sub> peaks are located at 642.6 and 654.2 eV, respectively. Although the observed peak positions are slightly different in the two spectra, a consistent spin-energy separation of 11.6 eV is observed between the Mn 2p<sub>3/2</sub> and Mn 2p<sub>1/2</sub> peaks. These results are also in accordance with the previously reported

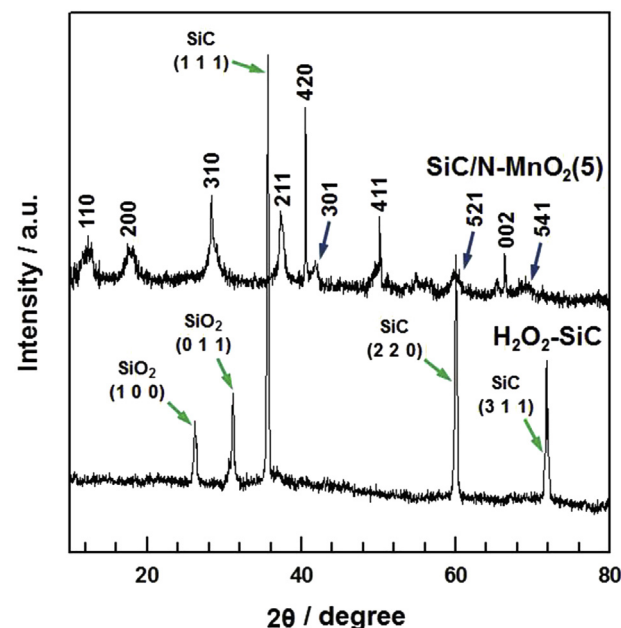


Fig. 2. XRD patterns of H<sub>2</sub>O<sub>2</sub>–SiC and SiC/N–MnO<sub>2</sub>(5).

**Table 2**

The C 1s peak position and the relative atomic percentages of various functional groups in HF–SiC and H<sub>2</sub>O<sub>2</sub>–SiC.

| Fitting of the C 1s peak binding energy [eV] (Relative atomic percentage [%]) |                                 |              |               |               |
|---|---------------------------------|--------------|---------------|---------------|
| Si–C  | SiO <sub>x</sub> C <sub>y</sub> | C–C          | C–OH/C–O–C    |               |
| HF–SiC  | 282.59 (33.4)                   | 283.47 (7.5) | 284.55 (59.1) | –             |
| H <sub>2</sub> O <sub>2</sub> –SiC  | 282.65 (28.9)                   | 283.56 (8.9) | 284.58 (41.6) | 286.24 (20.6) |

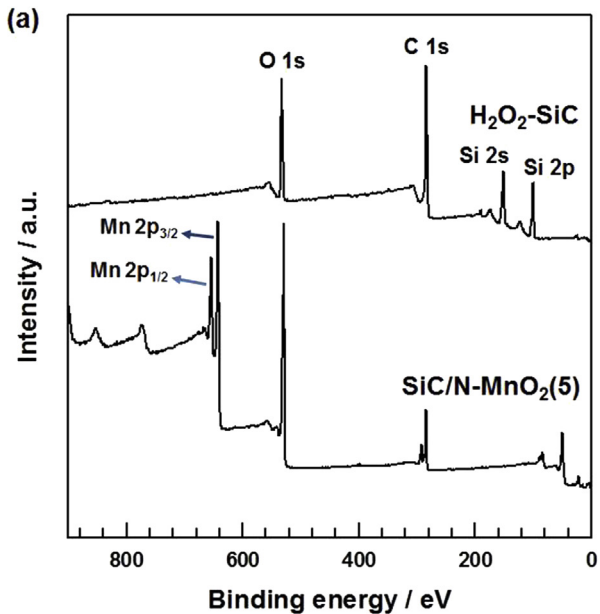


Fig. 3. (a) XPS wide scan survey spectra of  $\text{H}_2\text{O}_2\text{-SiC}$  and  $\text{SiC/N-MnO}_2(5)$ . (b) XPS spectra of Mn 2p peaks of the  $\text{SiC/N-MnO}_2(5)$  composite.

data for the Mn 2p<sub>3/2</sub> and Mn 2p<sub>1/2</sub> peaks of  $\text{MnO}_2$  nanoneedles [31].

The compositions of the as-prepared  $\text{SiC/N-MnO}_2(1)$  and  $\text{SiC/N-MnO}_2(5)$  composites are further investigated via TGA, as shown in Fig. 4. The experiments are performed at temperatures up to 800 °C under air flow at a heating rate of 10 °C min<sup>-1</sup>. Under these conditions,  $\text{HF-SiC}$  exhibits only 0.4% weight loss, whereas loss of mass associated with the adsorbed water is initiated upon heating below 100 °C in the case of  $\text{H}_2\text{O}_2\text{-SiC}$ , with a significant decrease in mass around 215 °C, which is ascribed to the evolution of CO and  $\text{CO}_2$  from  $\text{H}_2\text{O}_2\text{-SiC}$  due to the decomposition of oxygenated functional groups [33]. Moreover, nanoneedle  $\text{MnO}_2$  is converted into  $\text{Mn}_2\text{O}_3$  with an associated 14.7% weight loss [31]. Fig. 4 shows the representative TGA curves of  $\text{HF-SiC}$ ,  $\text{H}_2\text{O}_2\text{-SiC}$ ,  $\text{SiC/N-MnO}_2(1)$ ,  $\text{SiC/N-MnO}_2(5)$ , and  $\text{N-MnO}_2$ . The overall weight losses for  $\text{HF-SiC}$ ,  $\text{H}_2\text{O}_2\text{-SiC}$ ,  $\text{SiC/N-MnO}_2(1)$ ,  $\text{SiC/N-MnO}_2(5)$ , and  $\text{N-MnO}_2$  are 0.4%, 5.3%, 10.4%, 13.1%, and 14.7%, respectively. Accordingly, the mass ratios of  $\text{N-MnO}_2/(\text{H}_2\text{O}_2\text{-SiC})$  for  $\text{SiC/N-MnO}_2(1)$  and  $\text{SiC/N-MnO}_2(5)$  are derived to be 1.18/1 and 4.87/1, respectively. Thus, the  $\text{N-MnO}_2/(\text{H}_2\text{O}_2\text{-SiC})$  mass ratio increases with increasing  $\text{MnO}_2$  content in the  $\text{SiC/N-MnO}_2$  composites.

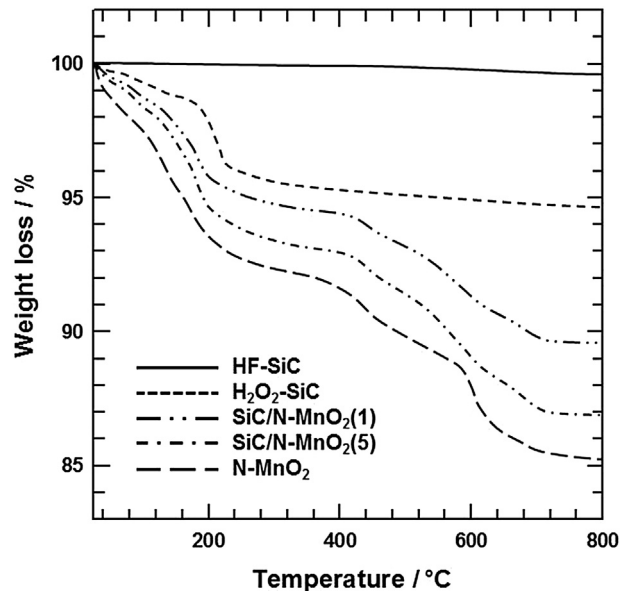
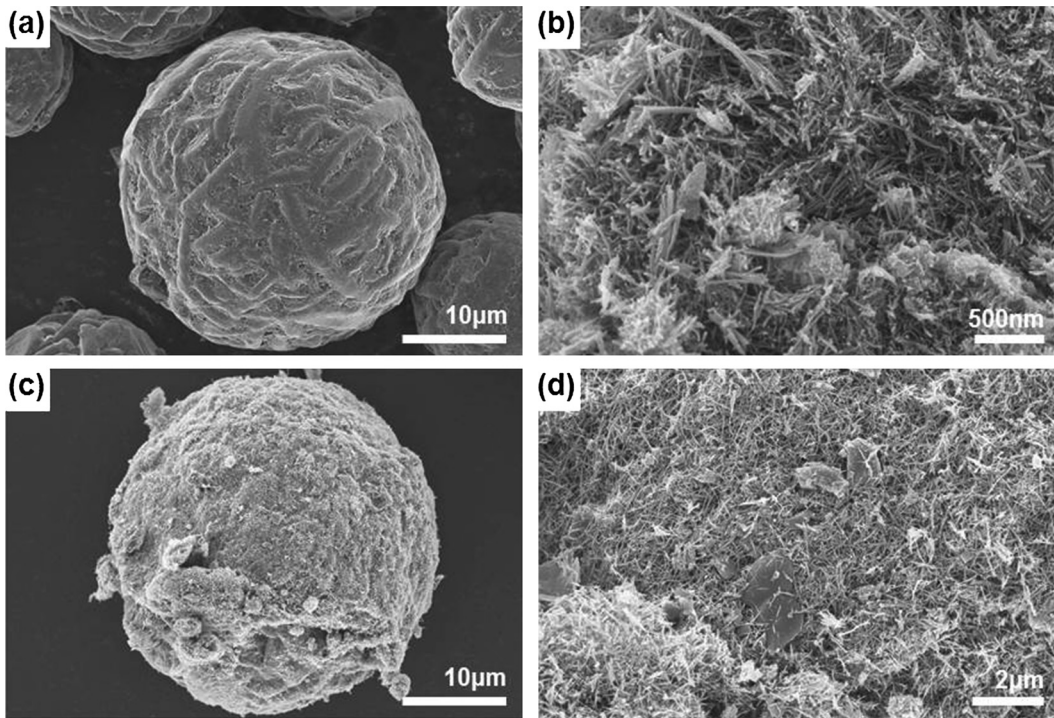


Fig. 4. TGA curves of  $\text{HF-SiC}$ ,  $\text{H}_2\text{O}_2\text{-SiC}$ ,  $\text{SiC/N-MnO}_2(1)$ ,  $\text{SiC/N-MnO}_2(5)$  and  $\text{N-MnO}_2$ .

$\text{MnO}_2$  are 0.4%, 5.3%, 10.4%, 13.1%, and 14.7%, respectively. Accordingly, the mass ratios of  $\text{N-MnO}_2/(\text{H}_2\text{O}_2\text{-SiC})$  for  $\text{SiC/N-MnO}_2(1)$  and  $\text{SiC/N-MnO}_2(5)$  are derived to be 1.18/1 and 4.87/1, respectively. Thus, the  $\text{N-MnO}_2/(\text{H}_2\text{O}_2\text{-SiC})$  mass ratio increases with increasing  $\text{MnO}_2$  content in the  $\text{SiC/N-MnO}_2$  composites.

The morphology and structure of the as-prepared composites are further studied using FE-SEM analysis. The FE-SEM images of  $\text{SiC}$ ,  $\text{MnO}_2$  nanoneedles, and the  $\text{SiC/N-MnO}_2(5)$  composite are shown in Fig. 5. The  $\text{SiC}$  particles (Fig. 5(a)) are spherical, and the average particle diameter is nearly 30  $\mu\text{m}$  with a rough surface morphology. Fig. 5(b) shows the interesting morphology of the as-obtained  $\text{MnO}_2$  nanoneedles, with diameters of 20–40 nm and lengths of 200–500 nm [34]. After reaction of  $\text{SiC}$  with  $\text{MnCl}_2 \cdot 4\text{H}_2\text{O}$  and  $\text{KMnO}_4$ ,  $\text{MnO}_2$  nanoneedles are formed on the  $\text{SiC}$  surface. Fig. 5(c) and (d) respectively present the low- and high-magnification FE-SEM images of the  $\text{SiC/N-MnO}_2(5)$  composite. Nanoneedle  $\text{MnO}_2$  is uniformly formed on the  $\text{SiC}$  surface. The oxygen-containing functional groups (epoxy and hydroxyl groups on the  $\text{SiC}$  surface), acting as the anchor sites, facilitate the homogeneous formation of nanostructures attached to the  $\text{SiC}$  surface [35]. The formation of homogeneously arrayed  $\text{MnO}_2$  nanoneedles on the  $\text{SiC}$  surface is attributed to the larger specific surface area of the exterior and interior pore surfaces of  $\text{SiC}$  that is accessible to the electrolyte ions and to the shorter transport/diffusion path lengths for both ions and electrons [36].

Cyclic voltammograms and galvanostatic charge/discharge measurements are utilized to evaluate the electrochemical properties of the as-prepared electrode. Fig. 6(a) shows the CV curves of the  $\text{SiC}$ ,  $\text{SiC/N-MnO}_2(1)$ , and  $\text{SiC/N-MnO}_2(5)$  electrodes, acquired at a scan rate of 10 mV s<sup>-1</sup> in 1 M  $\text{Na}_2\text{SO}_4$  electrolyte. The CV curve for the  $\text{SiC}$  electrode has a nearly ideal rectangular shape without obvious redox peaks, indicating that the composites exhibit ideal capacitive behavior [37]. The good capacitive properties of the  $\text{SiC}$  electrode are attributed to synergy between the electric double layer capacity, excellent electrical conductivity, and expansive electro-active areas. The  $\beta$ -polytype of  $\text{SiC}$  exhibits outstanding electronic conductivity because  $\beta$ - $\text{SiC}$  possesses the smallest bandgap ( $\sim 2.4$  eV) and one of the highest electron mobilities ( $\sim 800 \text{ cm}^2 \text{ V}^{-1} \text{ s}^{-1}$  in low-doped material) of all the known  $\text{SiC}$  polytypes [38]. Moreover, the



**Fig. 5.** (a) FE-SEM image of SiC particles. (b) FE-SEM image of MnO<sub>2</sub> nanoneedles. (c) Low-magnification FE-SEM image of SiC/N–MnO<sub>2</sub>(5). (d) High-magnification FE-SEM image of SiC/N–MnO<sub>2</sub>(5).

spherical morphology is beneficial for enhancing the surface area and forming pores that act as ion-buffering reservoirs, resulting in enhanced electric double layer capacity. Therefore, in the composites, SiC acts as a support for the formation of MnO<sub>2</sub> nanoneedles and as an electronic conductive channel, and the excellent interfacial contact between the MnO<sub>2</sub> nanoneedles and SiC is highly beneficial for fast transport of electrons throughout the electrode matrix. The integrated area of the CV curve of all the evaluated SiC/N–MnO<sub>2</sub> composite electrodes is clearly significantly greater than that of the SiC electrode, which results in excellent electrochemical performance, an observation that is attributed to the presence of the MnO<sub>2</sub> nanoneedles. The greatest advantage of MnO<sub>2</sub> is that it can facilitate pseudo-capacitive reactions and increase the surface area of the electrodes to enhance the charge storage process. Therefore, the presence of the homogeneously dispersed MnO<sub>2</sub> nanoneedles on the SiC/N–MnO<sub>2</sub> electrodes may maximize the pseudo-capacitive reactions as well as increase the specific area, which results in the formation of pores that act as ion-buffering reservoirs to improve the rate of diffusion of Na<sup>+</sup> ions [26]. Additionally, the dispersion generates good alignment of the nanoneedles allowing them to serve as well-ordered tunnels that are convenient for the insertion and extraction of Na<sup>+</sup> cations into and out of MnO<sub>2</sub>. Furthermore, the diffusion length over which Na<sup>+</sup> ions must travel during the charge/discharge process is significantly reduced by nanoscale MnO<sub>2</sub> particles, thus improving the electrochemical utilization of MnO<sub>2</sub> [39]. Moreover, the proposed mechanism for the charge storage of MnO<sub>2</sub>-based electrodes in a mild electrolyte involves rapid intercalation of alkali metal cations such as Na<sup>+</sup> into the electrode during reduction and deintercalation upon oxidation [40].



where X<sup>+</sup> = Na<sup>+</sup>, K<sup>+</sup>, and Li<sup>+</sup>. The proposed mechanism involved a redox reaction between trivalent and tetravalent Mn. Therefore, this redox reaction results in pseudocapacitance, which may

improve the supercapacitance. The MnO<sub>2</sub> redox reactions in the SiC/N–MnO<sub>2</sub> electrodes examined herein are evidenced by the distortion of the CV curves in the high-potential range, whereas the CV curve of the SiC electrode is characterized by a highly symmetrical rectangular shape. Compared with the SiC/N–MnO<sub>2</sub>(1) electrode, the integrated area of the CV curve of the SiC/N–MnO<sub>2</sub>(5) electrode is much larger due to the introduction of a much larger number of MnO<sub>2</sub> nanoneedles in the latter, as confirmed by TGA. To obtain more information on the capacitive performance of the prepared composites, the SiC/N–MnO<sub>2</sub>(5) electrode is subjected to detailed measurements. Fig. 6(b) shows the CV curves of the SiC/N–MnO<sub>2</sub>(5) electrode acquired at scan rates of 5, 10, 20, 50, and 100 mV s<sup>-1</sup> in 1 M Na<sub>2</sub>SO<sub>4</sub> electrolyte solution. The CV profiles retain a largely rectangular shape with high symmetry and do not show any signs of obvious distortion with increasing potential scan rate, indicating that the SiC/N–MnO<sub>2</sub>(5) electrode has ideal capacitive properties and excellent reversibility.

Galvanostatic charge/discharge measurements of the SiC, SiC/N–MnO<sub>2</sub>(1), and SiC/N–MnO<sub>2</sub>(5) electrodes are performed between -0.1 and 0.9 V, in a 1-M Na<sub>2</sub>SO<sub>4</sub> solution, at a current density of 10 mA cm<sup>-2</sup>. As illustrated in Fig. 7(a), the charge curves of the SiC/N–MnO<sub>2</sub>(1) and SiC/N–MnO<sub>2</sub>(5) electrodes during the charging and discharging steps are nearly symmetrical, with the corresponding discharge counterparts, albeit with a slight curvature, indicating pseudocapacitive and double layer contributions [26]. Moreover, further comparison of the discharge curves of the SiC/N–MnO<sub>2</sub> composite electrodes reveal that the discharge time of the SiC/N–MnO<sub>2</sub>(5) electrodes is significantly longer, consistent with the CV curve behavior, because the discharge time is directly proportional to the specific capacitance of the electrodes. A sudden decline in the potential at the very beginning of the constant current discharge is generally observed; this decrease has been designated as the IR drop. This decrease in potential has been attributed to the resistance of the electrolytes and the inner

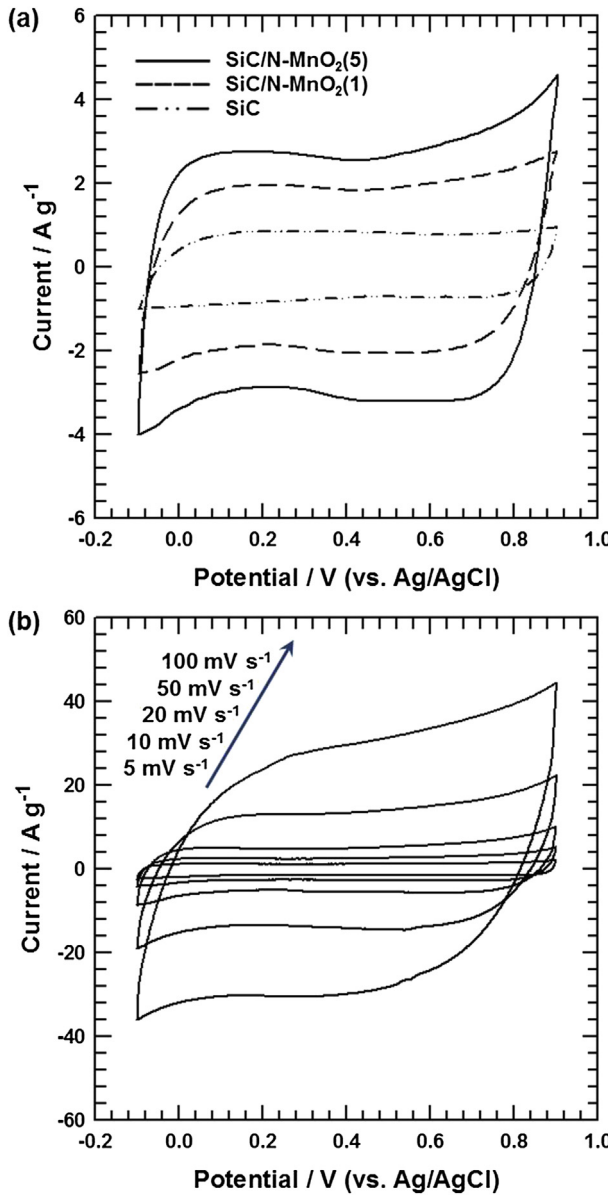


**Fig. 6.** (a) CV curves of SiC, SiC/N-MnO<sub>2</sub>(1) and SiC/N-MnO<sub>2</sub>(5) electrodes at a scan rate of 10 mV s<sup>-1</sup>. (b) CV curves of SiC/N-MnO<sub>2</sub>(5) electrode measured as different scan rates of 5, 10, 20, 50 and 100 mV s<sup>-1</sup>.

resistance of the electrode materials. The latter usually constitutes a greater contribution to the overall IR drop [41]. Assuming that the inner resistance is an intrinsic characteristic of the electrodes, the measured decrease in potential should be proportional to the discharge current. Fig. 7(b) shows the variation in the IR drop with discharge current for the SiC, SiC/N-MnO<sub>2</sub>(1), and SiC/N-MnO<sub>2</sub>(5) electrodes. The decrease in the potential increases linearly with current, and the slope of this linear relationship has been used to estimate the inner resistance of the electrodes [41]. The resistance increases as a function of the nanoneedle MnO<sub>2</sub> content, with resistances of 0.59, 1.55, and 2.12 Ω for the SiC, SiC/N-MnO<sub>2</sub>(1), and SiC/N-MnO<sub>2</sub>(5) electrodes, respectively. This result is partially affected by the low electrical conductivity of the SiC/N-MnO<sub>2</sub> electrodes after the formation of MnO<sub>2</sub>.

EIS measurements are performed for the SiC, SiC/N-MnO<sub>2</sub>(1), and SiC/N-MnO<sub>2</sub>(5) electrodes, as shown in Fig. 8. The EIS data are analyzed using Nyquist plots. The Nyquist plots consist of three

parts: (i) a semicircle in the high-to-medium frequency region, with the starting cross-point at the Z' axis, indicating the combined series resistance of the electrolyte, electrode, current collectors, electrode/current collector contact resistance, and the diameter of the semicircle representing the charge transport resistance ( $R_{ct}$ ); (ii) a straight line with a slope of 45° in the low-frequency range, which corresponds to the semi-infinite Warburg impedance resulting from the frequency dependence of ion diffusion/transport in the electrolyte; (iii) a vertical line at very low frequencies, caused by the accumulation of ions at the bottom of the pores of the electrode. The nearly vertical line indicates good capacitive behavior without diffusion limitations [42]. Comparison of the impedance plots of the SiC, SiC/N-MnO<sub>2</sub>(1), and SiC/N-MnO<sub>2</sub>(5) electrodes illustrates a major difference in the semicircle in the high-frequency range, which corresponds to the charge-transfer resistance ( $R_{ct}$ ), which is related to both the electrical

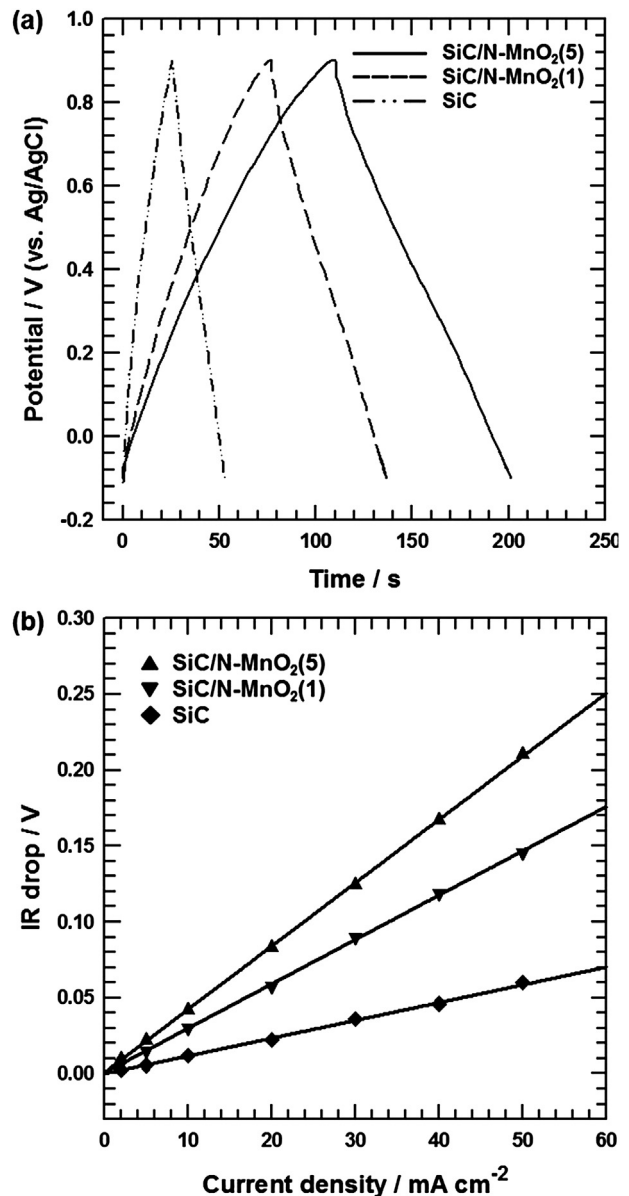


**Fig. 7.** (a) Galvanostatic charge/discharge curves of SiC, SiC/N-MnO<sub>2</sub>(1) and SiC/N-MnO<sub>2</sub>(5) electrodes at a current density of 10 mA cm<sup>-2</sup>. (b) Potential drop associated with SiC, SiC/N-MnO<sub>2</sub>(1) and SiC/N-MnO<sub>2</sub>(5) electrodes internal resistance (IR loss) vs. different discharge current densities.

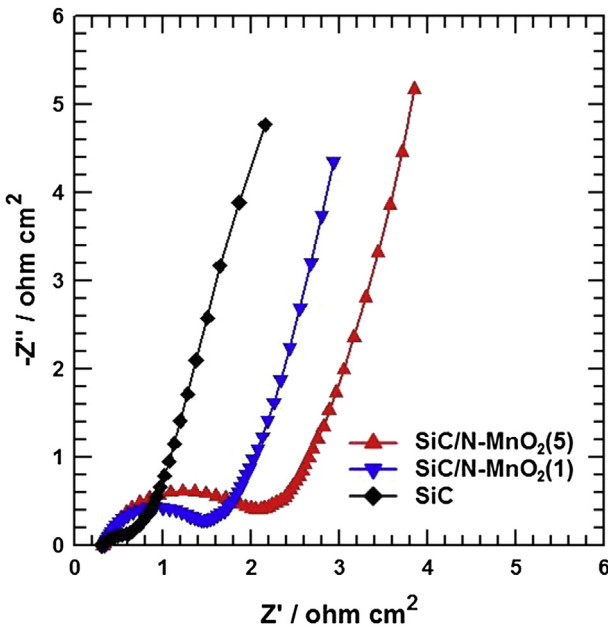


Fig. 8. Nyquist plots of SiC, SiC/N–MnO<sub>2</sub>(1) and SiC/N–MnO<sub>2</sub>(5) electrodes.

conductivity of the electrodes and the Faradaic reactions. The SiC/N–MnO<sub>2</sub>(5) electrode exhibits the highest  $R_{ct}$  value among the SiC/N–MnO<sub>2</sub> composite electrodes, corresponding to an increasing  $R_{ct}$  value with increasing MnO<sub>2</sub> content, which is confirmed by the TG analysis, as illustrated in Fig. 4 [43]. In general, the ESR coincides with the intercept of the semicircle at the middle frequencies, i.e., between the semicircle and the Warburg response, where the latter is located near the vertical line. The ESR is equal to the sum of the combined series resistance plus the charge-transfer resistance [44,45]. Therefore, the ESR values of SiC, SiC/N–MnO<sub>2</sub>(1), and SiC/N–MnO<sub>2</sub>(5) are 0.61, 1.53, and 2.23 Ω, respectively. These values agree with the results obtained from the IR drop. Furthermore, the straight lines at very low frequencies for all electrodes are nearly

vertical, indicating rapid ion diffusion in the electrolyte and adsorption on the electrode surface.

The specific capacitances ( $C_s$ ) are calculated from the CV curves using the following equation [46]:

$$C_s = \frac{1}{v(V_c - V_a)} \int_{V_a}^{V_c} I(V) dV \quad (2)$$

where  $C_s$  is the specific capacitance ( $F g^{-1}$ ),  $v$  is the potential scan rate ( $mV s^{-1}$ ),  $V_c - V_a$  represents the sweep potential range (V), and  $I(V)$  denotes the response current density ( $A g^{-1}$ ). Fig. 9 indicates the relationship between  $C_s$  and the scan rates of the SiC, SiC/N–MnO<sub>2</sub>(1), and SiC/N–MnO<sub>2</sub>(5) electrodes. The calculated  $C_s$  values of the SiC, SiC/N–MnO<sub>2</sub>(1), and SiC/N–MnO<sub>2</sub>(5) electrodes at 10  $mV s^{-1}$  are 72.4, 176.9, and 273.2  $F g^{-1}$ , respectively. The highest specific capacitance is achieved with the SiC/N–MnO<sub>2</sub>(5) electrode over the entire range of scan rates, which can be attributed to the intrinsic EDL capacitance of SiC in conjunction with the pseudocapacitive reaction due to the homogeneous dispersion of the nanosized MnO<sub>2</sub>. Moreover, the  $C_s$  values for all electrodes decreases steadily with increasing scan rate owing to the reduced access of ions to the active surface, especially with relatively slow faradic reactions. The pseudocapacitance due to the nanoneedle MnO<sub>2</sub> in the composite is calculated by subtracting the EDLC capacitance contribution from the SiC substrate using the following equation [31]:

$$C_{MnO_2} = (C_{SiC/MnO_2} - C_{SiC} \times SiC\%) / MnO_2\% \quad (3)$$

where  $C_{MnO_2}$ ,  $C_{SiC/MnO_2}$ , and  $C_{SiC}$  are the specific capacitance of nanoneedle MnO<sub>2</sub>, SiC/N–MnO<sub>2</sub> (SiC/N–MnO<sub>2</sub>(1) and SiC/N–MnO<sub>2</sub>(5) in this calculation), and SiC, respectively, and SiC% and MnO<sub>2</sub>% are the weight percentages of the SiC and nanoneedle MnO<sub>2</sub> in the composites. Given that the specific capacitance of the SiC electrode is 72.4  $F g^{-1}$  at a scan rate of 10  $mV s^{-1}$ , the specific capacitance of the nanoneedle MnO<sub>2</sub> is calculated to be 264.8 for SiC/N–MnO<sub>2</sub>(1) and 314.3  $F g^{-1}$  for SiC/N–MnO<sub>2</sub>(5). These results indicate that the introduction of a much larger amount of nanoneedle MnO<sub>2</sub> can enhance the redox reactions (as illustrated in Eq.

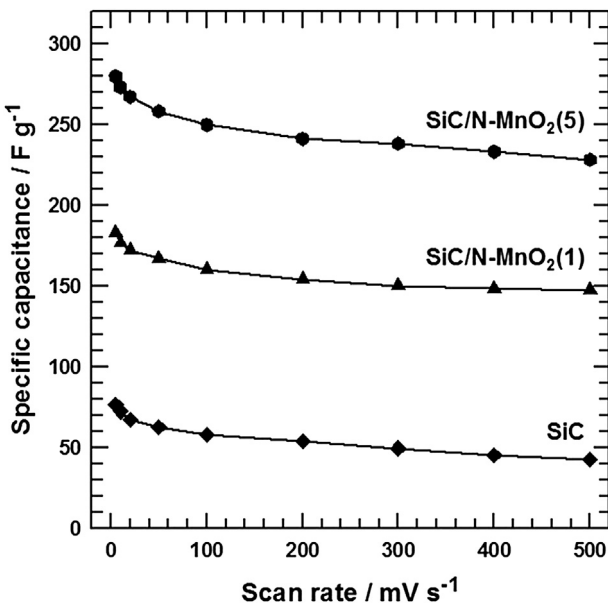


Fig. 9. Specific capacitance of SiC, SiC/N–MnO<sub>2</sub>(1) and SiC/N–MnO<sub>2</sub>(5) electrodes at different scan rates.

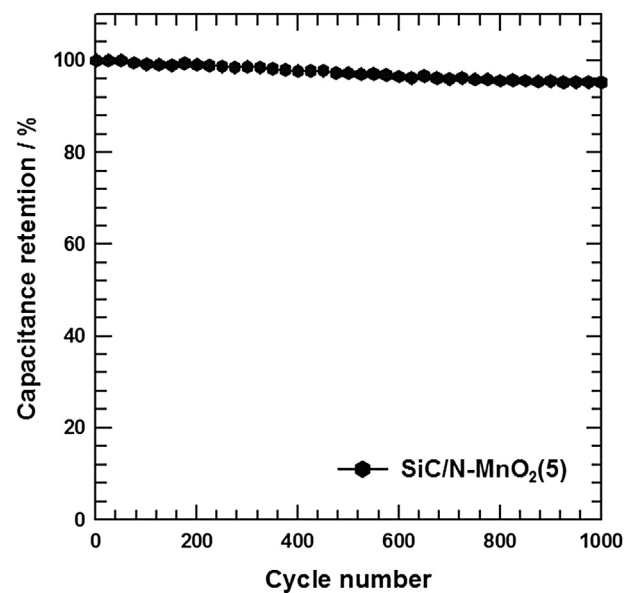


Fig. 10. Cycling stability of SiC/N–MnO<sub>2</sub>(5) electrode measured at 10  $mV s^{-1}$ .

(1)), resulting in pseudocapacitance that can improve the supercapacitance.

Cycle lifetime is particularly important for supercapacitor applications. Typical problems associated with  $\text{MnO}_2$ -based electrodes in aqueous electrolytic media include mechanical expansion of  $\text{MnO}_2$  during the ion insertion/deinsertion process,  $\text{MnO}_2$  detachment from the electrode surfaces, and dissolution of Mn into the electrolyte [47]. The cyclic stability of the  $\text{SiC}/\text{N}-\text{MnO}_2(5)$  electrode is evaluated over 1000 cycles at a scan rate of  $10 \text{ mV s}^{-1}$  using a potential window range between  $-0.1$  and  $0.9 \text{ V}$  Fig. 10 illustrates the specific capacitance retention as a function of cycle number. The  $\text{SiC}/\text{N}-\text{MnO}_2(5)$  electrode exhibits a specific capacitance loss of less than 4.7% after 1000 charge/discharge cycles, demonstrating its excellent capacity retention.

#### 4. Conclusions

$\text{SiC}/\text{N}-\text{MnO}_2$  composites were synthesized, and their structural characteristics and electro-chemical properties were evaluated for potential application in supercapacitors. The  $\text{SiC}/\text{N}-\text{MnO}_2$  composite prepared from  $\text{MnO}_2$  nanoneedles and  $\text{SiC}$  with different feeding ratios exhibits excellent electrochemical performance. The specific capacitance of the  $\text{SiC}/\text{N}-\text{MnO}_2(5)$  composite electrode at a scan rate of  $10 \text{ mV s}^{-1}$  was  $273.2 \text{ F g}^{-1}$ . The capacitance of the  $\text{SiC}/\text{N}-\text{MnO}_2(5)$  composite electrode decreases by only 4.7% from the initial capacitance after 1000 cycles, indicating excellent electrochemical stability. These encouraging results illustrate the exciting potential for development of high-performance electrical energy storage devices based on this  $\text{SiC}/\text{N}-\text{MnO}_2$  hybrid, prepared by a fast, cost-efficient, and environment-friendly method. Furthermore, this hybrid material strategy introduces possibilities for combination of silicon carbide with other redox pseudocapacitive materials in order to increase the energy density of supercapacitors.

#### Acknowledgments

This work was supported by the Technological Innovation R&D Program (S2085171) funded by the Small and Medium Business Administration (SMBA, Korea) and Basic Science Research Program through the National Research Foundation of Korea (NRF) funded by the Ministry of Education, Science and Technology (2012R1A1A2008884).

#### References

- [1] V. Subramanian, H. Zhu, R. Vajtai, P.M. Ajayan, B. Wei, *J. Phys. Chem. B* 109 (2005) 20207–20214.
- [2] A.L. Mohana, R.F. Estaline, A. Imran, J.S. Ramaprabhu, *Nanoscale Res. Lett.* 3 (2008) 145–151.
- [3] A.C.-G. Karina, L.-C. Monica, C.-P. Nieves, G.-R. Pedro, *Adv. Funct. Mater.* 15 (2005) 1125–1133.
- [4] J. Chow, R.J. Kopp, P.R. Portney, *Science* 302 (2003) 1528–1531.
- [5] Z. Wen, X. Wang, S. Mao, Z. Bo, H. Kim, S. Cui, G. Lu, X. Feng, J. Chen, *Adv. Mater.* 24 (2012) 5610–5616.
- [6] R. Kotz, M. Carlen, *Electrochim. Acta* 45 (2000) 2483–2498.
- [7] Z. Chen, Y. Qin, D. Weng, Q. Xiao, Y. Peng, X. Wang, H. Li, F. Wei, Y. Lu, *Adv. Funct. Mater.* 19 (2009) 3420–3426.
- [8] S. Bose, T. Kuila, A.K. Mishra, R. Rajasekar, N.H. Kim, J.H. Lee, *J. Mater. Chem.* 22 (2012) 767–784.
- [9] H. Jiang, J. Ma, C.Z. Li, *Adv. Mater.* 24 (2012) 4197–4202.
- [10] P. Simon, Y. Gogotsi, *Nat. Mater.* 7 (2008) 845–854.
- [11] S.L. Chou, J.Z. Wang, S.Y. Chew, H.K. Liu, S.X. Dou, *Electrochim. Commun.* 10 (2008) 1724–1727.
- [12] X.C. Dong, H. Xu, X.W. Wang, Y.X. Huang, Mary B.C. Park, H. Zhang, L.H. Wang, W. Huang, P. Chen, *ACS Nano* 6 (2012) 3206–3213.
- [13] S. Chen, J. Zhu, X. Wang, *J. Phys. Chem. C* 114 (2010) 11829–11834.
- [14] X. Xia, Q. Hao, W. Lei, W. Wang, D. Sun, X. Wang, *J. Mater. Chem.* 22 (2012) 16844–16850.
- [15] C. Xiang, M. Li, M. Zhi, A. Manivannan, N. Wu, *J. Power Sources* 226 (2013) 65–70.
- [16] J.W. Choi, J. McDonough, S. Jeong, J.S. Yoo, C.K. Chan, Y. Cui, *Nano Lett.* 10 (2010) 1409–1413.
- [17] John P. Alper, Maxime Vincent, Cario Carraro, Roya Maboudian, *Appl. Phys. Lett.* 100 (2012) 163901–163904.
- [18] John P. Alper, M.S. Kim, Maxime Vincent, Ben Hsia, Velimir Radmilovic, Cario Carraro, Roya Maboudian, *J. Power Sources* 230 (2013) 298–302.
- [19] X. Lu, G. Wang, T. Zhai, M. Yu, S. Xie, Y. Ling, C. Liang, Y. Tong, Y. Li, *Nano Lett.* 12 (2012) 5376–5381.
- [20] X. Lu, G. Wang, T. Zhai, M. Yu, J. Gan, Y. Tong, Y. Li, *Nano Lett.* 12 (2012) 1690–1696.
- [21] H. Zhang, T. Zhai, M. Yu, S. Xie, C. Liang, W. Zhao, S.C.I. Wang, Z. Zhang, X. Lu, *J. Mater. Chem. C* 1 (2013) 225–229.
- [22] S.B. Ma, K.W. Nam, W.S. Yoon, X.Q. Yang, K.Y. Ahn, K.H. Oh, K.B. Kim, *J. Power Sources* 178 (2008) 483–489.
- [23] S. Komaba, A. Ogata, T. Tsuchikawa, *Electrochim. Commun.* 10 (2008) 1435–1437.
- [24] S. Chen, J. Zhu, Q. Han, Z. Zheng, Y. Yang, X. Wang, *Cryst. Growth Des.* 9 (2009) 4356–4361.
- [25] S. Devaraj, N. Munichandraiah, *J. Phys. Chem. C* 112 (2008) 4406–4417.
- [26] S. Chen, J. Zhu, X. Wu, Q. Han, X. Wang, *ACS Nano* 4 (2010) 2822–2830.
- [27] M.J. Kim, Y.S. Hwang, K.C. Min, J.H. Kim, *Electrochim. Acta* 113 (2013) 322–331.
- [28] Y. Zhang, E.W. Shi, Z.Z. Chen, X.B. Li, B. Xiao, *J. Mater. Chem.* 16 (2006) 4141–4145.
- [29] Z. Liu, L. Ci, N.Y. Jin-Phillipp, M. Ruhle, *J. Phys. Chem. C* 111 (2007) 12517–12521.
- [30] R.P. Socha, K. Laajalehto, P. Nowak, *Colloids Surf. A* 208 (2002) 267–275.
- [31] L. Mao, K. Zhang, H. Chan, J. Wu, *J. Mater. Chem.* 22 (2012) 1845–1851.
- [32] C. Xu, X. Wang, J. Zhu, *J. Phys. Chem. C* 112 (2008) 19841–19845.
- [33] C. Xu, X. Wang, J. Zhu, X. Yang, L. Lu, *J. Mater. Chem.* 18 (2008) 5625–5629.
- [34] M.J. Kim, Y.S. Hwang, J.H. Kim, *Phys. Chem. Chem. Phys.* 16 (2014) 351–361.
- [35] M.J. Kim, Y.S. Hwang, J.H. Kim, *Chem. Eng. J.* 230 (2013) 482–490.
- [36] Z.S. Wu, W. Ren, D.W. Wang, F. Li, B. Liu, H.M. Cheng, *ACS Nano* 4 (2010) 5835–5842.
- [37] J. Yan, Z. Fan, T. Wei, W. Qian, M. Zhang, F. Wei, *Carbon* 48 (2010) 3825–3833.
- [38] J.B. Casady, R.W. Johnson, *Solid State Electron.* 39 (1996) 1409–1422.
- [39] M.J. Kim, Y.S. Hwang, J.H. Kim, *J. Power Sources* 239 (2013) 225–233.
- [40] S.B. Yoon, K.B. Kim, *Electrochim. Acta* 106 (2013) 135–142.
- [41] C.T. Hsieh, H. Teng, *Carbon* 40 (2002) 667–674.
- [42] T. Bordjiba, D. Belanger, *J. Electrochim. Soc.* 156 (2009) A378–A384.
- [43] Z. Li, J. Wang, S. Liu, X. Liu, S. Yang, *J. Power Sources* 196 (2011) 8160–8165.
- [44] Sanjib Biswas, Lawrence T. Drzal, *Chem. Mater.* 22 (2010) 5667–5671.
- [45] A. Di Fabio, A. Giorgi, M. Mastragostino, F. Soavi, *J. Electrochim. Soc.* 148 (2001) A845–A850.
- [46] X. Xie, L. Gao, *Carbon* 45 (2007) 2365–2373.
- [47] G. Xiong, K.P.S.S. Hembram, R.G. Reifenberger, T.S. Fisher, *J. Power Sources* 227 (2013) 254–259.